University of Central Lancashire
UCLan

Article

Non-volatile leaky integrate-and-fire neurons with domain walls in antiferromagnetic insulators

Austefjord, Johannes W., Brehm, Verena, Lepadatu, Serban and Qaiumzadeh, Alireza

Available at http://clok.uclan.ac.uk/44823/

Austefjord, Johannes W., Brehm, Verena, Lepadatu, Serban orcid iconORCID: 0000-0001-6221-9727 and Qaiumzadeh, Alireza (2022) Non-volatile leaky integrate-and-fire neurons with domain walls in antiferromagnetic insulators. Condensed Matter . (Submitted)

It is advisable to refer to the publisher's version if you intend to cite from the work.
10.48550/arXiv.2211.16845

For more information about UCLan's research in this area go to http://www.uclan.ac.uk/researchgroups/ and search for <name of research Group>.

For information about Research generally at UCLan please go to http://www.uclan.ac.uk/research/

All outputs in CLoK are protected by Intellectual Property Rights law, including Copyright law. Copyright, IPR and Moral Rights for the works on this site are retained by the individual authors and/or other copyright owners. Terms and conditions for use of this material are defined in the policies page.

CLoK
Central Lancashire online Knowledge
www.clok.uclan.ac.uk

CLoK
University of Central Lancashire's Institutional Repository

arXiv:2211.16845v1 [cond-mat.dis-nn] 30 Nov 2022

Non-volatile leaky integrate-and-fire neurons with domain walls in antiferromagnetic insulators

Johannes W. Austefjord‡

Center for Quantum Spintronics, Department of Physics, Norwegian University of Science and Technology, Trondheim, Norway

Verena Brehm§

Center for Quantum Spintronics, Department of Physics, Norwegian University of Science and Technology, Trondheim, Norway

Serban Lepadatu

Jeremiah Horrocks Institute for Mathematics, Physics and Astronomy, University of Central Lancashire, Preston, PR1 2HE, UK

Alireza Qaiumzadeh

Center for Quantum Spintronics, Department of Physics, Norwegian University of Science and Technology, Trondheim, Norway

Abstract. Despite the rapid development of powerful supercomputers in recent years, the human brain still has some abilities that outperform modern computers which are based on the von Neumann architecture. The human brain is much more energy efficient than state-of-the-art digital computers and can at the same time perform complex tasks such as pattern recognition. The brain-inspired neuromorphic computing paradigm is a promising path towards next generation analogue computers with fundamentally different architecture. The building blocks of the human brain are neurons with leaky integrate-and-fire mechanisms. In this work, using the advantage of antiferromagnetic insulators, we propose a non-volatile spintronic-based neuron. In our proposal, an antiferromagnetic domain wall in the presence of a magnetic anisotropy gradient mimics a biological neuron with leaky and integrative properties. This single neuron is controlled by polarized antiferromagnetic magnons, activated by either a magnetic field pulse or a spin transfer torque mechanism. We propose that this single neuron, based on antiferromagnetic insulators, is faster and more energy efficient than other metallic ferromagnetic-based neurons.

‡ These authors contributed equally
§ These authors contributed equally

1. Introduction

Modern electronic digital computers are designed based on the socalled von Neumann computing architecture. They rely on central processing units (CPU), built upon complementary metal-oxide-semiconductor (CMOS) transistors [1]. In contrast to that, inspired by the human brain and its complex neural network, novel energy efficient analogue computing architectures with strongly interconnected processing elements have been proposed that lead to the emerging technology of neuromorphic computing and engineering [2–5].

The conventional CPU-based von Neumann computing architecture is faster than the current state of the art neuromorphic computing, but the latter offers more energy efficient data processing. To achieve even more energy efficiency as well as faster data processing in neuromorphic computing architecture, it was proposed very recently that neuromorphic principles may be implemented in spintronic-based nanodevices. This leads to the emerging field of the neuromorphic spintronics [6]. In spintronic-based nanotechnology, the intrinsic spin angular momentum of electrons, rather than their charge, may be used for data storage and processing. The magnetic insulators that host magnons and various topological magnetic textures are key ingredients for efficient data processing and information storage [7]. Consequently, ubiquitous Joule heating arising from electron scatterings in metals and semiconductors is avoided. Furthermore, recent theoretical and experimental advances in spintronics have shown that antiferromagnetic (AFM) systems have even much more advantages compared to their ferromagnetic (FM) counterparts [8, 9]. The absence of parasitic stray fields, operating frequencies in THz regime compared to GHz in FM systems, and their abundance in nature, make AFM-based spintronics a promising candidate for hardware implementation of the next generation of ultrafast, low-energy cost, and miniaturized non-volatile neuromorphic chips [10–13].

Spiking neural networks (SNNs) are a class of neuromorphic computing architecture that mimic human neural networks [14]. These spiking neural networks may support energy efficient operation of deep neural networks. One of the most successful spiking neural network models is the leaky integrate-and-fire (LIF) model [15]. This model resembles the spiking behavior of a neuron at the onset of critical accumulating stimuli and its slow decay to the equilibrium state until the next spike [16]. LIF may be used as the building block of neuromorphic chips [17].

In this paper, we propose a non-volatile AFM-based single neuron with leaky integrate-and-fire properties. The state of this neuron is encoded in the position of a magnetic domain wall (DW), which is displaced by travelling magnons in the material. Leaky behaviour is ensured by a nonuniform magnetic anisotropy profile.

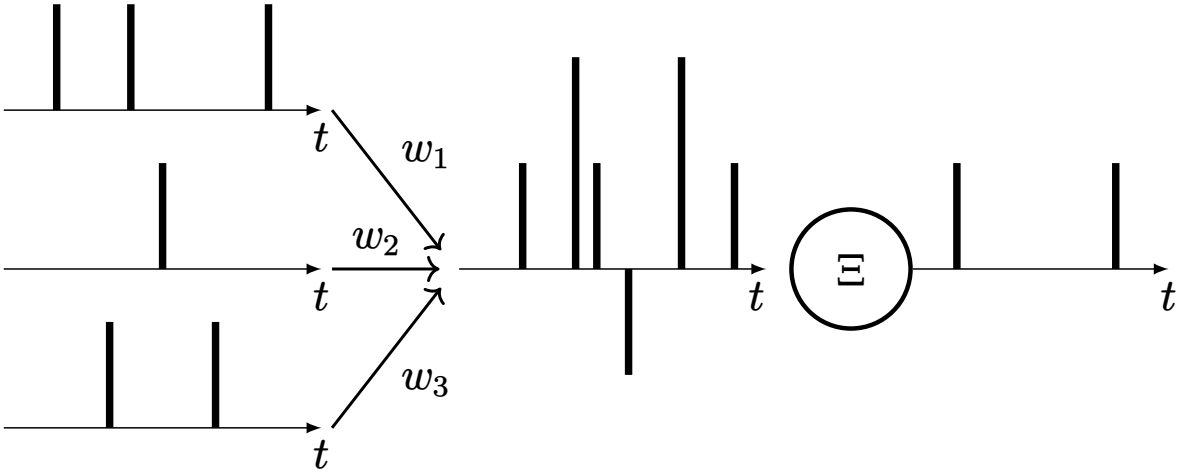

Figure 1: Schematic of a simple spiking neuron. Three spike trains or three synapses lead to a spiking neuron Ξ. The spike trains are multiplied by weights w_i and merged before they get sent into Ξ. A non-linear function determines whether the neuron should fire as a consequence of stimuli from its synapses. Figure inspired by [19].

2. Theory of Neural Networks

In this section, we briefly summarize the key elements and ingredients of SNN and LIF single neuron models.

2.1. Spiking Neural Networks

A SNN takes the inspiration of human brain activity into computer science one step further than other models of artificial neural networks, like feedforward neural networks [18]. Information in this model is encoded as spike trains; c.f., binary information coding, used in conventional computers. The network has an explicit time dependency and the system is event-driven. We first give a brief mathematical description of the SNN model. A generic spiking neuron Ξ is represented in Fig. 1. Let V be a finite set of spiking neurons, connected by a set of $E \subseteq V \times V$ synapses. For each synapse $\langle i, j\rangle \in E$ between presynaptic neuron j and postsynaptic neuron i there is associated a response function ϵ_{ij} and a weight w_{ij}. The state variable of i^{th} neuron, $u_i(t)$, is then given by [15, 18],

$$u_i(t) = \delta(t - t_i^{(f)}) + \sum_j \sum_f w_{ij}\epsilon_{ij}(t - t_j^{(f)}) + u_0. \tag{1}$$

Here u_0 is the equilibrium potential, i.e. the value of $u_i(t)$ when no stimuli has affected the neuron and $t_j^{(f)}$ indicates the firing times, where f is the label of each spike. In general the firing time $t = t_i^{(f)}$ of a neuron i is set when $u_i(t)$ reaches a threshold value

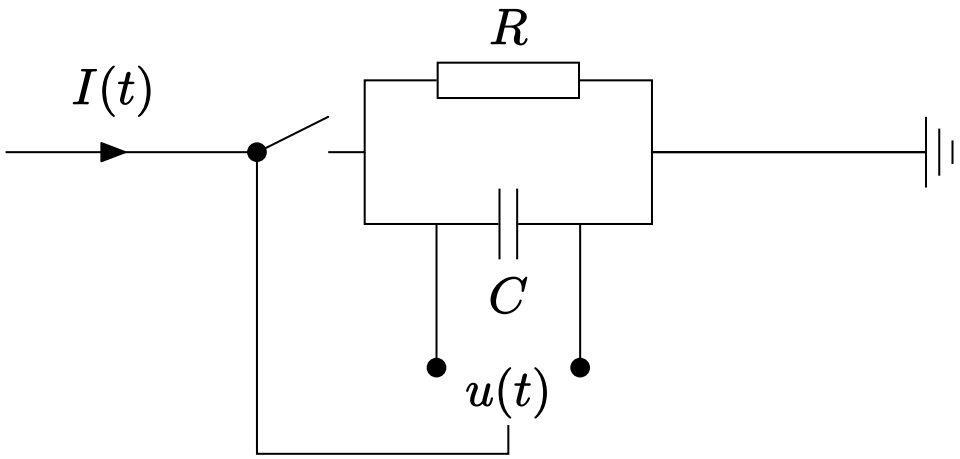

Figure 2: Leaky integrate-and-fire circuit. A capacitor, C, and a resistor, R, are connected in parallel. The voltage over the capacitor $u(t)$ integrates the current input, while it leaks to ground. When $u(t)$ reaches a threshold value, a switch controlling the input wire is flipped, stopping new currents into the system for a refractory period. During the refractory period charge is completely depleted from the capacitor. Figure inspired by [15].

$u_{\text{threshold}}$,

$$\begin{aligned} &u_i(t) = u_{\text{threshold}} \quad \wedge \quad \text{sgn}(u_i(t) - u_0)\frac{du_i(t)}{dt} > 0 \\ &\implies t = t_i^{(f)}, \end{aligned} \tag{2}$$

where $\text{sgn}(x)$ is the sign function and $\epsilon_{ij}(t - t_j^{(f)})$ determines the response for postsynaptic neuron i from stimuli from presynaptic neuron j. Once a spike is initiated, $u_i(t)$ is immediately reset to u_0. Equation 1 can therefore be used to model a human neuron: after the action potential in a neuron has been raised and neurotransmitters have been transferred, it relaxes back to its ground state until the next activation happens.

It is worth noting that Eq. (1) assumes no time delay as signals travel the synapses. This could easily be added with a delay time for each synapse [20].

2.2. Leaky Integrate-and-Fire Neurons

The rather general Eq. (1) can be used to model a variety of neuron models. LIF models are one of the most prominent neuron types [15]. It can be modelled by a resistor–capacitor circuit (RC) circuit as shown in Fig. 2. The neuron voltage corresponds to the capacitor voltage $u_i(t)$. The LIF model is described by a differential equation,

$$\tau\frac{du_i}{dt} = -u_i(t) + RI_i(t), \tag{3}$$

where $\tau = RC$ is the time constant of the RC circuit, and R and C are the resistance and capacitance of the resistor and capacitor, respectively. The incoming current $I_i(t)$

is,

$$I_i(t) = \sum_j w_{ij} \sum_f \delta(t - t_j^{(f)}). \tag{4}$$

The weights w_{ij} determine the connection strength from presynaptic neuron j to postsynaptic neuron i. The sum $\sum_f$ is over all presynaptic spike times (f).

The purpose of the LIF model is to describe how the spiking neuron Ξ behaves as a function of external stimuli, or captures the dynamics of the ϵ_{ij} response function in Eq. (1). The LIF model has a memory of previous inputs $I_i(t)$, stored on the capacitor. The resistor ensures that this memory only is short term. As before, a spike is fired when $u_i(t)$ reaches a threshold value by Eq. (2). A generalization to a non-linear leaky integrate-and-fire model gives

$$\tau \frac{du_i}{dt} = F(u_i) + G(u_i) I_i(t), \tag{5}$$

where the functions $F(u_i)$ and $G(u_i)$ are arbitrary functions. It is worth noting that Eq. (1) describes $u_i(t)$ as a function of time since the last input, while Eqs. (3) and (5) are implicit equations.

3. Non-volatile Spintronic-Based LIF Neurons

In this section, we introduce our proposal for a non-volatile LIF neuron, implemented with a magnetic DW in an AFM insulator.

3.1. AFM Model

We consider a two-sublattice AFM insulator nanoribbon, modelled by the following potential-energy density for each sublattice,

$$\begin{aligned} \mathcal{U}_i(\boldsymbol{m}_i, \nabla \boldsymbol{m}_i; \boldsymbol{r}) =& A(\boldsymbol{\nabla} \boldsymbol{m}_i)^2 + 4A_{\mathrm{h}} \boldsymbol{m_i} \cdot \boldsymbol{m_j} - \mu_0 M_{\mathrm{s}} \boldsymbol{m}_i \cdot \boldsymbol{h} - K_{\mathrm{easy}} (\boldsymbol{m}_i \cdot \mathrm{e}_{\mathrm{easy}})^2 \\ &+ K_{\mathrm{hard}} (\boldsymbol{m}_i \cdot \mathrm{e}_{\mathrm{hard}})^2 + D \boldsymbol{m}_i \cdot (\nabla \times \boldsymbol{m}_i) + \eta_i \frac{D_h}{2} \boldsymbol{d}_h \times \boldsymbol{m}_j, \end{aligned} \tag{6}$$

where $i \neq j \in \{\mathrm{A}, \mathrm{B}\}$ refer to two AFM sublattices. Within a micromagnetic framework [21, 22], all magnetic contributions in a unit cell with volume V_0 are averaged to a macrospin magnetic moment $\boldsymbol{M}$, with a saturation magnetization value $M_s = |\boldsymbol{M}|$. The unit vector of magnetization direction is $\boldsymbol{m} = \boldsymbol{M}/M_s$. A and A_{h} parameterize the AFM exchange stiffness and the homogeneous Heisenberg exchange interaction, respectively, $K_{\mathrm{easy\ (hard)}} > 0$ parameterizes single ion easy (hard) axis anisotropy energy along the $\mathrm{e}_{\mathrm{easy\ (hard)}}$ direction, $\boldsymbol{h}$ is the applied magnetic field, D is the strength of the inhomogeneous bulk-type Dzyaloshinskii-Morya interaction (DMI) while D_h is the homogeneous DMI along the direction $\boldsymbol{d}_h$ with a sublattice-dependent sign $\eta_{A(B)} = +(-)1$.

We assume the AFM insulator supports a rigid magnetic domain wall (DW) that connects two uniform AFM domains, see Fig. 3. Within the collective coordinate

Table 1: Numerical parameters used for micromagnetic simulations.

Quantity	Value	Unit
Length of AFM (L_x)	500	nm
Width of AFM (L_y)	20	nm
Height of AFM (L_z)	4	nm
Inhomogeneous exchange stiffness (A)	1	$\mathrm{pJ\,m^{-1}}$
Homogeneous exchange energy (A_h)	-200	$\mathrm{kJ\,m^{-3}}$
Easy-axis anisotropy energy (K_{easy})	20	$\mathrm{kJ\,m^{-3}}$
Hard-axis anisotropy energy (K_{hard})	10	$\mathrm{kJ\,m^{-3}}$
Saturation magnetization (M_s)	2.1	$\mathrm{kA\,m^{-1}}$
Gilbert damping parameter (α)	0.002	1
Inhomogeneous bulk DMI (D)	0–250	$\mathrm{\mu J\,m^{-2}}$
Homogeneous DMI (D_h)	2	$\mathrm{kJ\,m^{-3}}$
Applied magnetic field frequency (ω)	62.5	$\mathrm{rad\,ps^{-1}}$

approximation [23], the position of the DW center is considered as a dynamical variable $\mathcal{X}_{\mathrm{DW}}$. In order to control the equilibrium position of DW center, the spatial profile of the anisotropy energy density K can be tuned by electric field via voltage-controlled magnetic anisotropy (VCMA) effect [24–28] or strain-induced magnetic anisotropy [29–32]. We model a spatially varying anisotropy as,

$$K(\boldsymbol{x}) = K_0 \left[\left(\frac{x}{L_x} - \frac{2}{3} \right)^2 + 1 \right], \tag{7}$$

where L_x is the length of the AFM nanoribbon along the x-direction. This magnetic anisotropy profile creates a magnetic potential well along the x- direction with a minimum value K_0 at $\mathcal{X}_0 = 2L_x/3$. The AFM DW is at its minimum energy if the DW center is placed at this minimum $\mathcal{X}_0$. If there is no spatial dependent magnetic anisotropy, the system has translation invariance and AFM DWs have no preferred equilibrium position. The spatial dependent of $K(\boldsymbol{x})$ ensures that the AFM DW always relaxes back toward its ground-state position $\mathcal{X}_0$ in the absence of stimuli, giving the neuron a leaky behaviour.

3.2. AFM DWs as LIF Neurons

Our proposed system is schematically presented in Fig. 3. It consists of an AFM insulator stripe, an injector (modelling the receptor of a human neuron) that excites magnons in the AFM insulator via either a circularly polarized magnetic field pulse or current-induced (anomalous) spin Hall torque mechanism [33, 34], and a detector (modelling the transmitter). The detector measures the passing DW via inverse (anomalous) spin Hall effect of the injected spin-pumping signal [33–37]. In a series

of neuron networks, this detector or transmitter must be connected to the injector or receptor of the following neuron. At a given set of material parameters and excitation strength, the position of the detector determines the neuron threshold potential.

AFM DWs are 1D particle-like magnetic solitons that connect two magnetic domains in magnetic materials. It was recently shown that the position of a DW in an AFM insulator is controllable through magnon-DW interactions [38]. The position of AFM DW may be used as a state variable for the LIF neuron, $u(t) \longrightarrow \mathcal{X}_{\rm DW}$ [39].

In the following, two generic magnetic geometries for possible implementation of LIF neurons are investigated and compared, which we will call in-plane (IP) and out-of-plane (OOP), referring to their magnetic ground-state orientation. In order to model these two magnetic states using the potential energy density expression given by Eq. (6), we set $\boldsymbol{e}_{\rm easy} = \hat{e}_x$ and $\boldsymbol{e}_{\rm hard} = \hat{e}_z$ in IP case, while for OOP, we set $\boldsymbol{e}_{\rm easy} = \hat{e}_z$ and $\boldsymbol{e}_{\rm hard} = \hat{e}_x$. Therefore, in the IP geometry, the magnetic ground state lies along the direction of magnon propagation, i.e., the x axis, while in the OOP geometry, the magnetic ground state is normal to the direction of magnon propagation. In both cases, we assume the homogeneous DM vector lies parallel to the hard axis, $\boldsymbol{d}_h \parallel \boldsymbol{e}_{\rm hard}$.

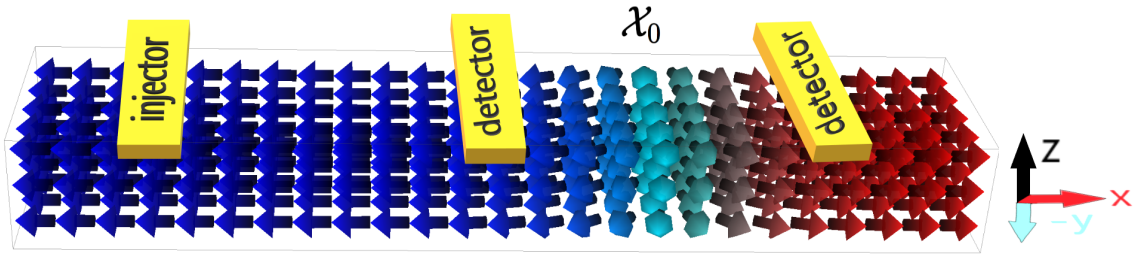

Figure 3: Schematic setup of the AFM-based single neuron proposal in the IP geometry. There are two domains in the AFM stripe, represented by the Néel vectors in blue and red. The two domains are connected by a DW texture in turquoise. On top of the AFM stripe, an injector is placed at the left side as a source of magnons and two detectors are placed right and left of the equilibrium position of the DW, the latter shown by $\mathcal{X}_0$.

4. Equation of Motions for AFM Systems

The dynamics of the normalized sublattice magnetic moments $\boldsymbol{m}_{i\in\{\rm A,\,B\}}(\boldsymbol{r},t)$, in finite temperature, is given by the coupled stochastic Landau-Lifshitz-Gilbert (sLLG) equations,

$$\frac{\partial \boldsymbol{m}_i}{\partial t} = -|\gamma_{\rm e}|\mu_0 \boldsymbol{m}_i \times (\mathcal{H}_i + \mathcal{H}_i^{th}) + \alpha \boldsymbol{m}_i \times \frac{\partial \boldsymbol{m}_i}{\partial t} + \boldsymbol{T}(\boldsymbol{r},t), \tag{8}$$

with the electron gyromagnetic ratio γ_e, the vacuum permeability μ_0 and the Gilbert damping constant α. The sublattice-dependent effective magnetic field $\mathcal{H}_i = -(\mu_0 M_{\rm s})^{-1}\delta U/\delta \boldsymbol{m}_i$, is given by the functional derivative of the total potential energy

$U[\boldsymbol{m}_{\mathrm{A}}, \boldsymbol{m}_{\mathrm{B}}; \boldsymbol{r}, t] = \int d\boldsymbol{r} \sum_i \mathcal{U}_i(\boldsymbol{m}_i, \nabla \boldsymbol{m}_i; \boldsymbol{r})$. Finite temperature dynamics is captured by adding an uncorrelated white noise effective magnetic field $\mathcal{H}_i^{th}(t)$, derived by fluctuation-dissipation theorem [21]. The current-induced spin transfer torque and magnetic field torque are denoted by $\boldsymbol{T}$ in the sLLG equation. $\boldsymbol{T}(\boldsymbol{r}, t)$ is finite only in the injector region and during the excitation period.

To solve coupled sLLG equations for our AFM system, we use the software Boris Computational spintronics [22]. The list of parameters, used in the micromagnetic simulations, is given in the Table 1.

5. Results

In this section, we show how our proposed non-volatie AFM-based LIF neuron works. As we mentioned earlier, AFM DWs are displaced by AFM magnons that can be generated by either magnetic field pulses or by (anomalous) spin Hall torque. We present the results for both magnon excitation methods in the following subsections.

5.1. Magnon-Induced AFM DW Motion by Magnetic Fields

Magnetic field pulses may excite monochromatic AFM magnons with certain polarizations. It was theoretically shown that these AFM magnons can displace AFM textures in opposite directions depending on their polarizations, values of DMI, and the Gilbert damping parameter [38, 40, 41].

Table 2: Four-stage protocol for magnon-induced DW movement, induced by a transverse magnetic field pulse.

Stage	Magnetic Field Pulse	Polarization
Excitation 1	$\boldsymbol{H}_{IP}(t) = (0, H_0 \cos\omega t, H_0 \sin\omega t)$ $\boldsymbol{H}_{OOP}(t) = (H_0 \cos\omega t, H_0 \sin\omega t, 0)$	↺
Relaxation 1	$H_0 = 0$	-
Excitation 2	$\boldsymbol{H}_{IP}(t) = (0, H_0 \sin\omega t, H_0 \cos\omega t)$ $\boldsymbol{H}_{OOP}(t) = (H_0 \sin\omega t, H_0 \cos\omega t, 0)$	↻
Relaxation 2	$H_0 = 0$	-

In this part, first, we demonstrate the control of the AFM DW in our setup. To do so, a four-stage protocol is run, see Table 2: In the first excitation stage, a small amplitude transverse magnetic field pulse with circular polarization is applied in the injector region to excite the AFM magnon eigenmodes in the magnetic layer. Afterwards, the magnetic field pulse is turned off and the system may relax back to its ground state in the first relaxation stage. Then, in the second excitation stage, the magnetic field pulse is applied again but with the opposite helicity. Finally, it is turned off again in the second relaxation stage. In Fig. 4, we present snapshots of magnon-induced AFM DW

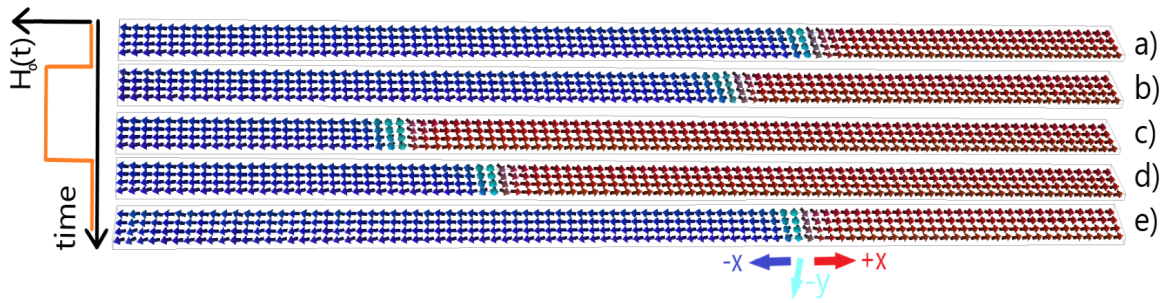

Figure 4: Snapshots of all-magnonic DW motion through an AFM-based neuron in the IP configuration with magnetic field pulse excitation. In (a), the DW is at equilibrium position $\mathcal{X}_{DW} = \mathcal{X}_0$, set by the magnetic anisotropy profile. Once a left-handed magnetic field pulse with strength H_0 is turned on, left-handed AFM magnons are excited at the injector. As a result, the DW moves towards the magnon source, panels (b) and (c). After switching the magnetic field off, the DW relaxes back to its equilibrium position, panels (d) and (e). The illustrated movement corresponds to the first excitation stage followed by the first relaxation stage in our protocol. We set $D = 150\,\mu\mathrm{J\,m^{-2}}$ in this case.

motion in an IP geometry for one excitation followed by one relaxation stage: while the magnetic field is turned on, the AFM DW travels from its equilibrium position (Fig. 4a) towards the left (Figs. 4b and 4c). Once the magnetic field is turned off, it relaxes back toward its equilibrium position (Figs. 4d and 4e).

By tuning the excitation strength and the distance of the detector from the magnetic anisotropy minimum, one can set the threshold for the firing mechanism. Depending on the strength of the DMI D, the DW surface can be tilted. This DMI-induced tilting was also reported in ferromagnetic DWs [42].

5.2. Direction and amplitude of the DW displacement

In this part, we show that the movement of AFM DWs can be controlled by demand, which makes them more flexible than their ferromagnetic counterpart. Besides the excitation strength (here the magnetic field strength), the magnon helicity, and the inhomogeneous DMI strength have a major impact on the DW displacement. In Fig. 5 the trajectory of the AFM DW center in the IP geometry (Fig. 5a) and OOP (Fig. 5b) is shown during the four-stage protocol, see Table 2. The orange areas in the plots sketch when and where the magnetic field pulse is applied while arrows indicate the helicity of the magnetic field pulse. The color map refers to the strength of the inhomogeneous bulk DMI, starting from dark blue for $D = 0$ and increasing over green to yellow for $D = 250\,\mu\mathrm{J\,m^{-2}}$ ($D = 200\,\mu\mathrm{J\,m^{-2}}$) for the IP (OOP) geometry. Every single line represents one DW trajectory at a given set of parameters. For example, at an intermediate DMI strength, the dark green curve in the IP case (Fig. 5a), the DW moves towards the injector during the first excitation stage (0–25 ps), then relaxes back

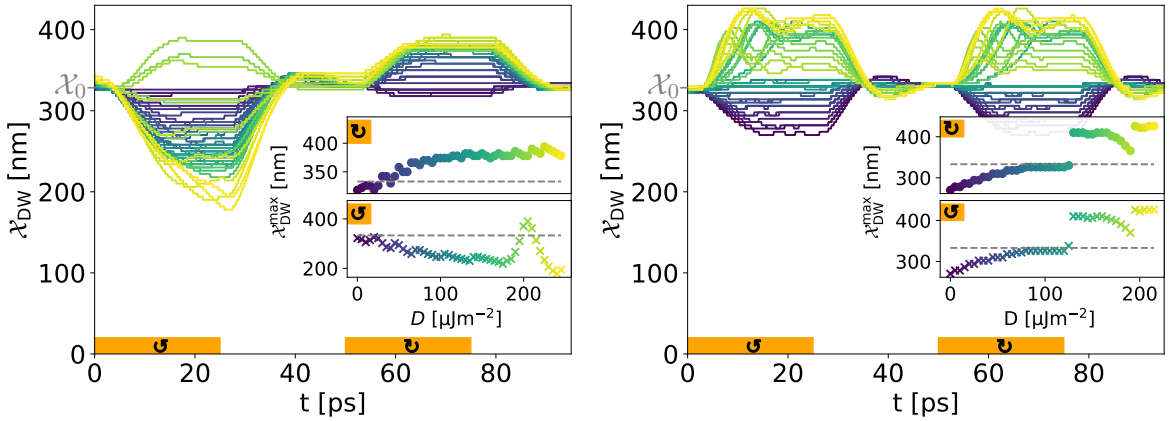

(a) IP geometry (b) OOP geometry

Figure 5: DMI-dependent all-magnonic AFM DW movement. Left- and right-handed AFM magnons are excited with polarized magnetic field pulses, see the orange area. In the IP geometry (a) the direction and amplitude of the DW motion can be tuned by DMI strength and the helicity of excited magnons. However, the direction of AFM DW motion in the OOP geometry (b) is independent of the magnon helicity. The strength of DMI is encoded by colors, from lowest $D = 0$ in blue to highest in yellow, see the insets. In the insets, the maximal displacements of AFM DWs, $\mathcal{X}_{\mathrm{DW}}^{\mathrm{max}}$, are shown for each excitation stage (crosses for the first and points for the second excitation stage).

to equilibrium position (35–50 ps), and in the second excitation stage with opposite helicity the AFM DW is pushed away from the injector (50–75 ps) before relaxing back to the equilibrium position again.

The first difference between the two cases is the helicity dependency of AFM DW motion. The displacement of an AFM DW in the OOP geometry is insensitive to the polarization of excited AFM magnon, while the displacement of an AFM DW in the IP case is helicity dependent.

Figure 5 shows that in the OOP geometry, only the strength of the inhomogeneous DMI determines the direction of the DW motion, but in the IP geometry, both the strength of the inhomogeneous DMI and the helicity of the excited magnons set the direction of AFM DW displacement.

The amplitude and direction of the maximum displacement of the AFM DW center, $\mathcal{X}_{\mathrm{DW}}^{\mathrm{max}}$, show a complicated relation with inhomogeneous DMI strength, see the insets in Fig. 5a and 5b. Recent theoretical studies have shown that, in the presence of an inhomogeneous DMI, several torques and forces act on the AFM DW, and thus the competition between them determines the direction and amplitude of the DW displacement [38].

5.3. LIF Behavior of AFM DWs

As we discussed earlier, biological neurons have LIF characteristics: if the input signal (or the sum of input spikes) reaches a threshold, the neuron fires, and then relaxes back to its ground state. In this part, we demonstrate that our proposed setup indeed can mimic the LIF behavior. In Fig. 6a the time-dependent AFM DW position in the IP geometry is shown, excited with three successive short magnetic field pulses. One single pulse is not strong enough to move the AFM DW to the detector while three pulses can move the DW toward the detector, where it triggers a spike in the read-out (see Fig. 6b, more explanation in the next section). This is a demonstration of the integrative-and-fire behavior of our proposed non-volatile spintronic-based neuron. The DW relaxes back to its equilibrium position that represents the required leaky characteristic.

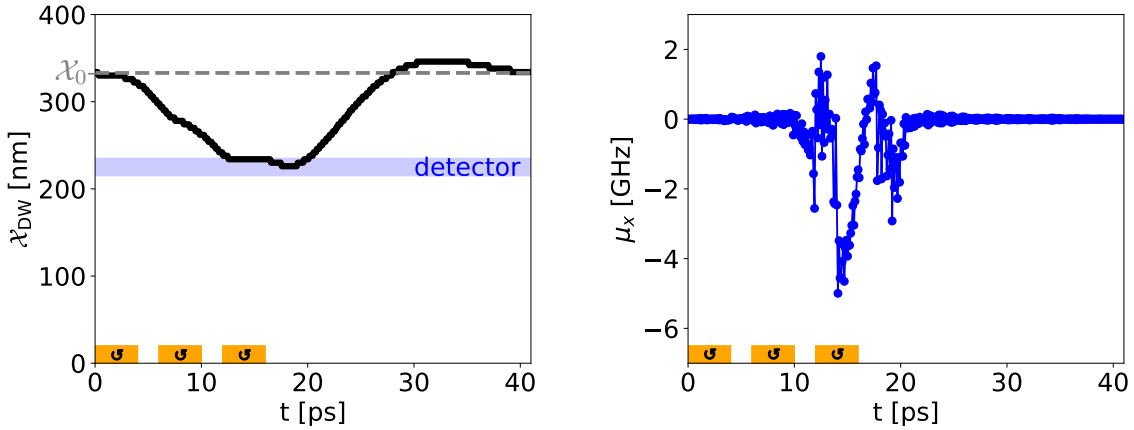

(a) Trajectory of the AFM DW (b) Spin-pumping signal at the detector

Figure 6: Leaky integrate-and-fire behavior of the all-magnonic AFM DW motion in the IP geometry with a DMI strength of $D = 150\,\mu J\,m^{-2}$. (a) The integration of three separate pulses, denoted by orange areas, provides enough energy to pull the DW away from its equilibrium position, denoted by the gray dashed line, to the detector, denoted by the blue area. This is the realization of the integrate-and-fire characteristic of LIF model. After the last pulse, the AFM DW relaxes back to the equilibrium position, which represents the leaky behavior of the single neuron. (b) An impulse-like signal is fired when the DW pass the detector. This spike, generated when the synaptic inputs to the neuron reach a certain threshold value, represents the neuron action potential.

5.4. Electrical Readout of the AFM DW Position

A detector on top of the AFM stripe measures the passing of the AFM DW by converting the spin-pumping signal, induced by AFM DW dynamics, to an electric voltage via either the inverse spin Hall effect [43] or recently discovered the inverse anomalous spin Hall effect [34]. In the former case, the detector is a nonmagnetic heavy metal and can only measure the component of spin-pumping signal parallel to the interface. In the latter

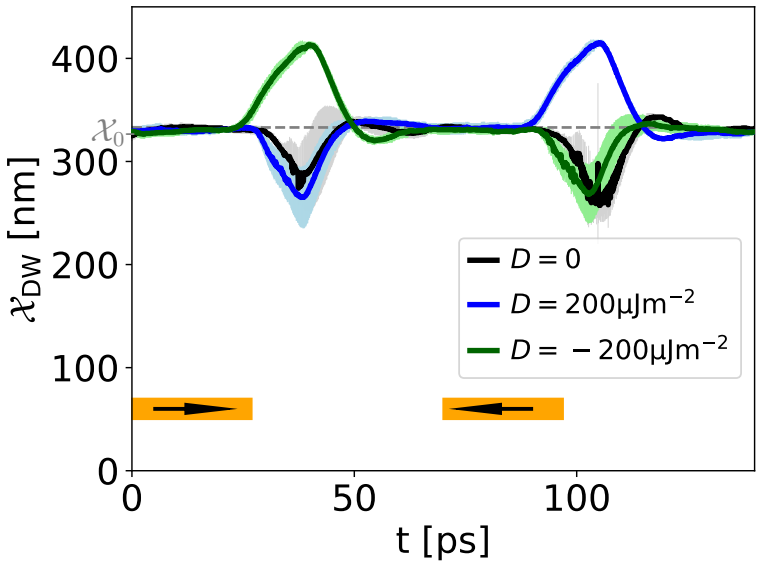

Figure 7: Electrical control of the AFM DW motion in the IP geometry. The orange areas depict the injector region that excites magnons via spin transfer torque pulses with two opposite spin torques, indicated by the arrow directions, at a finite temperature. Each trajectory is computed from an ensemble average over ten realizations, and the uncertainty environment represents the standard deviation. The equilibrium position of DW at $\mathcal{X}_0$ is denoted by a horizontal gray dashed line.

case, the detector is a ferromagnetic metal with a strong spin-orbit coupling that can measure different components of the spin-pumping signal.

The interfacial spin accumulation that arises from the DW-dynamics-induced spin-pumping, is given by [35, 44],

$$\boldsymbol{\mu}(t) := G_r^{\uparrow\downarrow} \Big\langle \sum_{i=\mathrm{A,\ B}} \big(\boldsymbol{m}_i(t,\boldsymbol{r}) \times \dot{\boldsymbol{m}}_i(t,\boldsymbol{r})\big) \Big\rangle, \tag{9}$$

where $G_r^{\uparrow\downarrow}$ is the real part of the spin mixing conductance [45] and $\langle ... \rangle$ denotes spatial average over the detector interface region.

In Fig. 6b, the temporal evolution of the spin accumulation signal $\mu_x(t)$ is presented for the IP geometry. In this example, as shown in Fig. 6a and described in the previous section, an AFM DW is pulled towards the detector with several small pulses. At the detector, the spin-pumping signal Eq. (9) is recorded over time. We subtract the background signal caused by the pumped magnons to find the filtered spin pumping signal arising from the AFM DW dynamics (blue curve). This signal clearly shows a maximum at around $t = 18\,\mathrm{ps}$, which is when the AFM DW passes underneath the detector.

5.5. Magnon-Induced AFM-DW Motion by Spin Hall Torque

Depending on the application, it might be an advantage to have an artificial single neuron that operates only electrically. To show our proposed setup has also all-electrical functionality, we replace the incident magnetic field pulse with a spin torque that results from a current-induced (anomalous) spin Hall torque in a non magnetic (magnetic) heavy-metal lead on top of the AFM at finite temperature. Through the (anomalous) spin Hall effect, a charge current in the injector is converted to a spin accumulation at the interface of the heavy metal and the AFM insulator. A nonequilibrium spin density with spin angular momentum along the easy-axis anisotropy may excite incoherent magnons in the AFM insulator via an interfacial spin transfer torque at finite temperature [33,46]. The helicity of excited magnons is controlled by the charge current direction and consequently the sign of the spin transfer torque.

Figure 7 represents the displacement of an AFM DW in the IP geometry. Similar to the four-stage protocol used before, we run the following stages: After initialization of the DW in its equilibrium position $\mathcal{X}_0$, the spin transfer torque is turned on for 25 ps as the first excitation stage, and then turned off for the first relaxation stage. In Fig. 7 we see that the time interval between turning on the injector and the DW motion is much bigger compared to the previous case, where magnons were excited by a magnetic field, see Fig. 5. This is because the spin transfer torque excitation mechanism needs time to build up enough magnons in the system.

In the second excitation stage, we change the sign of the spin accumulation and thus spin transfer torque in the injector, which is equivalent to reversing the direction of the charge current in the heavy metal layer. In Fig. 7, three AFM DW trajectories for different inhomogeneous DMI strengths are shown. Since temperature is finite, we perform an ensemble average for each AFM DW trajectory. The uncertainty environment for each line represents the standard deviation of the data set. In the absence of DMI (black line), the direction of spin accumulation does not have an impact on the DW motion direction and the DW is pulled towards the injector in both cases. This is consistent with our previous result for magnon-induced by magnetic field case in which the direction of AFM DW motion was helicity independent in the absence of inhomogeneous DMI. Turning the DMI on, however, leads to helicity dependent DW motion.

6. Summary and Concluding Remarks

Brain-inspired neuromorphic computing and engineering mimic biological nervous systems to overcome the von Neumann bottleneck. The building block of biological neural networks is the single neuron. In this paper, we have proposed a non-volatile, low-energy cost, and fast operating single neuron, which is based on a DW texture in an AFM insulator with an anisotropy gradient. Our proposed AFM-based neuron shows a leaky integrated-fire behavior, which is characteristic of biological neurons.

This single neuron is activated by AFM magnons, which can be excited at the source region by either magnetic field pulse or spin transfer torque mechanism. The source region that injects magnons into the system resembles a dendrite in a nerve cell. Our proposed single neuron has two detectors that act as transmitters and will be connected to neighboring neurons. These transmitters resemble synaptic terminals of neurons. In general, one can replace the AFM DW in our setup with topologically stable AFM skyrmions as well. Synchronization and functionality of the connected single neurons remain as an important open question that should be explored further theoretically and experimentally in next studies.

Acknowledgment

This project has been supported by the Norwegian Financial Mechanism Project No. 2019/34/H/ST3/00515, "2Dtronics"; and partially by the Research Council of Norway through its Centres of Excellence funding scheme, Project No. 262633, "QuSpin".

References

[1] Mahmoud A, Ciubotaru F, Vanderveken F, Chumak A V, Hamdioui S, Adelmann C and Cotofana S 2020 J. Appl. Phys. 128 161101 URL http://arxiv.org/abs/2006.12905

[2] Christensen D V, Dittmann R, Linares-Barranco B, Sebastian A, Gallo M L, Redaelli A, Slesazeck S, Mikolajick T, Spiga S, Menzel S, Valov I, Milano G, Ricciardi C, Liang S J, Miao F, Lanza M, Quill T J, Keene S T, Salleo A, Grollier J, Marković D, Mizrahi A, Yao P, Yang J J, Indiveri G, Strachan J P, Datta S, Vianello E, Valentian A, Feldmann J, Li X, Pernice W H P, Bhaskaran H, Furber S, Neftci E, Scherr F, Maass W, Ramaswamy S, Tapson J, Panda P, Kim Y, Tanaka G, Thorpe S, Bartolozzi C, Cleland T A, Posch C, Liu S, Panuccio G, Mahmud M, Mazumder A N, Hosseini M, Mohsenin T, Donati E, Tolu S, Galeazzi R, Christensen M E, Holm S, Ielmini D and Pryds N 2022 Neuromorph. Comput. Eng. 2 022501 URL https://dx.doi.org/10.1088/2634-4386/ac4a83

[3] Liu D, Yu H and Chai Y 2020 Adv. Intell. Syst. 3 2000150 URL https://onlinelibrary.wiley.com/doi/10.1002/aisy.202000150

[4] Rao A, Plank P, Wild A and Maass W 2022 Nat. Mach. Intell. 4 467 URL https://www.nature.com/articles/s42256-022-00480-w

[5] Levya W B and Calvert V G 2021 Proc. Natl. Acad. Sci. U.S.A. 118 e2008173118

[6] Grollier J, Querlioz D, Camsari K Y, Everschor-Sitte K, Fukami S and Stiles M D 2020 3 360 URL https://www.nature.com/articles/s41928-019-0360-9

[7] Brataas A, van Wees B, Klein O, de Loubens G and Viret M 2020 Phys. Rep. 885 1–27 ISSN 0370-1573 spin Insulatronics URL https://www.sciencedirect.com/science/article/pii/S0370157320302933

[8] Jungwirth T, Marti X, Wadley P and Wunderlich 2016 Nat. Nanotechnol. 11 231 URL https://www.nature.com/articles/nnano.2016.18

[9] Rezende S M, Azevedo A and Rodríguez-Suárez R L 2019 J. Appl. Phys. 126 151101 URL https://doi.org/10.1063/1.5109132

[10] Kurenkov A, Fukami S and Ohno H 2020 J. Appl. Phys. 128 010902 URL https://aip.scitation.org/doi/10.1063/5.0009482

[11] Zhang S and Tserkovnyak Y 2020 Phys. Rev. Lett. 125 207202 URL https://link.aps.org/doi/10.1103/PhysRevLett.125.207202

[12] Bradley H, Louis S, Trevillian C, Quach L, Bankowski E, Slavin A and Tyberkevych V 2022 URL https://arxiv.org/abs/2208.06565
[13] Bindal N, Ian C A C, Lew W S and Kaushik B K 2021 Nanotechnology 32 215204 URL https://dx.doi.org/10.1088/1361-6528/abe261
[14] Maass W 1997 Neural Netw. 10 1659–1671 URL https://www.sciencedirect.com/science/article/pii/S0893608097000117
[15] Gerstner W and Kistler W M 2002 Spiking Neuron Models: Single Neurons, Populations, Plasticity (Cambridge University Press)
[16] Stein R B 1965 Biophys. J. 5 173–194 URL https://www.sciencedirect.com/science/article/pii/S0006349565867091
[17] Stoliar P, Tranchant J, Corraze B, Janod E, Besland M P, Tesler F, Rozenberg M and Cario L 2017 Adv. Funct. Mater. 27 1604740 URL https://onlinelibrary.wiley.com/doi/abs/10.1002/adfm.201604740
[18] Maass W Neural Netw. 10 1659 URL https://www.sciencedirect.com/science/article/pii/S0893608097000117
[19] Jang H, Skatchkovsky N and Simeone O IEEE Commun. Lett. 25 1736 URL https://ieeexplore.ieee.org/document/9317739
[20] Bohte S M, Kok J N and La Poutré H Neurocomputing (Amsterdam) 48 17 URL https://www.sciencedirect.com/science/article/pii/S0925231201006580
[21] Etz C, Bergqvist L, Bergman A, Taroni A and Eriksson O 2015 J. Phys. Condens. Matter 27 243202 URL https://iopscience.iop.org/article/10.1088/0953-8984/27/24/243202
[22] Lepadatu S J. Appl. Phys. 128 243902 URL https://aip.scitation.org/doi/full/10.1063/5.0024382
[23] Tveten E G, Qaiumzadeh A, Tretiakov O A and Brataas A 2013 Phys. Rev. Lett. 110 127208 URL https://link.aps.org/doi/10.1103/PhysRevLett.110.127208
[24] Rana B and Otani Y 2019 Commun. Phys. 2 90 URL http://www.nature.com/articles/s42005-019-0189-6
[25] Ma C, Zhang X, Xia J, Ezawa M, Jiang W, Ono T, Piramanayagam S N, Morisako A, Zhou Y and Liu X 2018 Nano Lett. 19 353 URL https://doi.org/10.1021%2Facs.nanolett.8b03983
[26] Yu G, Upadhyaya P, Li X, Li W, Kim S K, Fan Y, Wong K L, Tserkovnyak Y, Amiri P K and Wang K L 2016 Nano Lett. 16 1981 URL https://doi.org/10.1021/acs.nanolett.5b05257
[27] Skowroński W, Nozaki T, Shiota Y, Tamaru S, Yakushiji K, Kubota H, Fukushima A, Yuasa S and Suzuki Y 2015 Appl. Phys. Express 8 053003 URL https://dx.doi.org/10.7567/APEX.8.053003
[28] Kawabe T, Yoshikawa K, Tsujikawa M, Tsukahara T, Nawaoka K, Kotani Y, Toyoki K, Goto M, Suzuki M, Nakamura T, Shirai M, Suzuki Y and Miwa S 2017 Phys. Rev. B 96 220412 URL https://link.aps.org/doi/10.1103/PhysRevB.96.220412
[29] Herklotz A, Gai Z, Sharma Y, Huon A, Rus S F, Sun L, Shen J, Rack P D and Ward T Z 2018 Adv. Sci. 5 1800356 URL https://onlinelibrary.wiley.com/doi/abs/10.1002/advs.201800356
[30] Belyaev B A, Izotov A V, Solovev P N and Boev N M 2020 Phys. Status Solidi RRL 14 1900467 URL https://onlinelibrary.wiley.com/doi/abs/10.1002/pssr.201900467
[31] Ebrahimian A, Dyrdał A and Qaiumzadeh A 2022 URL https://arxiv.org/abs/2209.04527
[32] Vishkayi S I, Torbatian Z, Qaiumzadeh A and Asgari R 2020 Phys. Rev. Materials 4 094004 URL https://link.aps.org/doi/10.1103/PhysRevMaterials.4.094004
[33] Lebrun R, Ross A, Bender S A, Qaiumzadeh A, Baldrati L, Cramer J, Brataas A, Duine R A and Kläui M 2018 Nature 561 222
[34] Das K S, Liu J, van Wees B J and Vera-Marun I J 2018 Nano Lett. 18 5633 URL https://doi.org/10.1021/acs.nanolett.8b02114
[35] Cheng R, Xiao J, Niu Q and Brataas A 2014 Phys. Rev. Lett. 113 057601 URL https://link.aps.org/doi/10.1103/PhysRevLett.113.057601
[36] Mal'shukov A G 2022 URL https://arxiv.org/abs/2211.01195
[37] Pham V T, Zahnd G, Marty A, Savero Torres W, Jamet M, Noël P, Vila L and Attané J P 2016 Appl. Phys. Lett. 109 192401 URL https://doi.org/10.1063/1.4967171

[38] Qaiumzadeh A, Kristiansen L A and Brataas A 2018 Phys. Rev. B 97 020402 URL https://link.aps.org/doi/10.1103/PhysRevB.97.020402
[39] Agrawal A and Roy K 2019 IEEE Trans. Magn. 55 1 URL https://ieeexplore.ieee.org/document/8552401
[40] Tveten E G, Qaiumzadeh A and Brataas A 2014 Phys. Rev. Lett. 112 147204 URL https://link.aps.org/doi/10.1103/PhysRevLett.112.147204
[41] Khoshlahni R, Qaiumzadeh A, Bergman A and Brataas A 2019 Phys. Rev. B 99 054423 URL https://link.aps.org/doi/10.1103/PhysRevB.99.054423
[42] Boulle O, Rohart S, Buda-Prejbeanu L D, Jué E, Miron I M, Pizzini S, Vogel J, Gaudin G and Thiaville A 2013 Phys. Rev. Lett. 111(21) 217203 URL https://link.aps.org/doi/10.1103/PhysRevLett.111.217203
[43] Sinova J, Valenzuela S O, Wunderlich J, Back C H and Jungwirth T 2015 Rev. Mod. Phys. 87(4) 1213–1260 URL https://link.aps.org/doi/10.1103/RevModPhys.87.1213
[44] Reitz D, Li J, Yuan W, Shi J and Tserkovnyak Y 2020 Phys. Rev. B 102(2) 020408 URL https://link.aps.org/doi/10.1103/PhysRevB.102.020408
[45] Tserkovnyak Y, Brataas A and Bauer G E W 2002 Phys. Rev. Lett. 88 117601 URL https://link.aps.org/doi/10.1103/PhysRevLett.88.117601
[46] Lebrun R, Ross A, Gomonay O, Baltz V, Ebels U, Barra A L, Qaiumzadeh A, Brataas A, Sinova J and Kläui M 2020 Nat. Commun. 11 6332 ISSN 2041-1723 URL http://www.nature.com/articles/s41467-020-20155-7